Streak instability in viscoelastic Couette flow

L. Biancofiore,[1,2] L. Brandt,[3] and T. A. Zaki[4,*]

[1]*Department of Mechanical Engineering, Imperial College London, Exhibition Road, South Kensington, London SW7 2AZ, United Kingdom*

[2]*Department of Mechanical Engineering, Bilkent University, 06800 Ankara, Turkey*

[3]*Linné Flow Centre and SeRC (Swedish e-Science Research Centre), KTH Mechanics, SE-10044 Stockholm, Sweden*

[4]*Department of Mechanical Engineering, Johns Hopkins University, 3400 North Charles Street, Baltimore, Maryland 21218-2681, USA*

(Received 7 November 2016; published 28 April 2017)

The secondary instability of nonlinear streaks and transition to turbulence in viscoelastic Couette flow are studied using direct numerical simulations. Viscoelasticity is modeled using the FENE-P constitutive equations. Both the polymer concentration β and Weissenberg number Wi are varied in order to assess their effects on transition at moderate Reynolds number. The base streaks are obtained from nonlinear simulations of the Couette flow response to a streamwise vortex. We select the initial amplitude of the vortex which yields a desired maximum amplitude of the nonlinear streaks during their temporal evolution. The development of streaks in both Newtonian and non-Newtonian flows is primarily due to the action of streamwise vorticity onto the mean shear. In the viscoelastic case, it is also affected by the polymer torque, which opposes the vorticity and becomes more pronounced at large Weissenberg number. Streaks with the same maximum streamwise velocity perturbation can therefore have different total kinetic energy at higher Weissenberg number. At every streak amplitude of interest, harmonic forcing is introduced along the transverse direction to trigger the secondary instability and breakdown to turbulence. We demonstrate that the critical amplitude of the forcing, A_d, increases at large Weissenberg number. The degree of stabilization due to elasticity depends on the initial streak intensity, $A_{s,\mathrm{in}}$. For weak streaks the critical amplitude for secondary instability is more sensitive to Wi than for strong ones. This is explained by the existence of two different mechanisms that can trigger transition to turbulence. The perturbation to weak streaks is initially stabilized by the polymer torque which acts to oppose the amplification of wall-normal vorticity and, as a result, delays breakdown to turbulence. The secondary instability of strong streaks, on the other hand, is more immune to this stabilizing influence of the polymer.

DOI: 10.1103/PhysRevFluids.2.043304

I. INTRODUCTION

In transitional wall-bounded shear flows, streaks are often a precursor to breakdown to turbulence [1]. These streaks are narrow regions of excess or defect streamwise velocity elongated in the streamwise direction. They are generated by streamwise vortices via the so-called lift-up effect, or vorticity tilting [2–4]. Tilting in this context refers to the generation of wall-normal vorticity due to the perturbation strain rate which tilts the vorticity of the mean flow, i.e., the mean spanwise vorticity, into the wall-normal direction. The large energy amplifications associated with streak growth, of the order of the square of the Reynolds number, are explained by the strongly non-normal nature of the linearized Navier-Stokes operator for shear flows.

Among the different studies of streak instability in Newtonian fluids, Cossu *et al.* [5] considered Couette flow and sought amplitude threshold for the streak breakdown. They concluded that the critical amplitude of the perturbations (sinuous in their case) increases when the streak amplitude

*Corresponding author: t.zaki@jhu.edu

decreases. For strong streaks, breakdown is triggered by a secondary modal instability [6–8] while for small amplitude streaks transition is triggered by a two-step process in which the vortex tilting mechanism plays a role starting from the transient streamwise vortices induced by the sinuous forcing [9]. The streaks are initially distorted by the sinuous perturbation, but after a short period they reach a maximum in their energy and return to a nearly stable state. However, they ultimately reach a higher amplitude and break down to turbulence. This process was previously described by Waleffe [10] for a generic shear flow.

In contrast to the wealth of studies focusing on Newtonian streaks and their secondary instability, there are relatively fewer efforts dedicated to the influence of fluid elasticity on (i) the growth of the streaks and (ii) their secondary instability. Whether elasticity is stabilizing or destabilizing to shear flows depends on the particular flow configuration and parameters. For example, it can promote or suppress absolute instability in spatially developing mixing layers [11] and jets [12]. The linear analysis by Jovanović and Kumar [13] showed that polymer stretching in elasticity-dominated flows can lead to streaks that are phenomenologically similar to those generated by lift-up in inertial Newtonian flows [13,14]. Whatever their origin, when streaks are present they can introduce streamline curvature that can be host for new elastic instabilities [15]. In direct numerical simulations (DNSs) of bypass transition in polymeric channel flow, Agarwal, Brandt, and Zaki [16] found that the polymers weaken the primary streaks and prolong the transition process.

Page and Zaki [17] analyzed the linear evolution of streaks in polymeric Couette flow. They identified three classes of streaks: (i) the quasi-Newtonian class, which includes streaks whose evolution collapses onto the Newtonian behavior when relaxation is either very fast or slow; (ii) the elastic class, in which the streaks can reach very large amplitude even in the absence of inertia [18,19]; and (iii) a class of streaks that undergo cycles of reenergization within an envelope of decay, and which take place when the solvent diffusion and relaxation time scales are commensurate.

The secondary instability of streaks in viscoelastic flow has not been examined, and the present work aims to address this gap. We analyze the canonical configuration of viscoelastic Couette flow distorted by a primary streak and examine its secondary instability. We first analyze the nonlinear evolution of the primary streaks generated by introducing a streamwise vortex. Afterwards, we assess the secondary instability of the streaks by focusing on the transition to turbulence triggered by a sinuous disturbance.

The paper is organized as follows. In Sec. II we introduce the governing equations, the numerical method, and the simulation setup. The amplification of the primary streaks is studied in Sec. III, followed by the transition to turbulence due to the streak instability in Sec. IV. Finally, conclusions are drawn in Sec. V.

II. GOVERNING EQUATIONS AND SIMULATIONS SETUP

A. Governing equations

The incompressible dimensionless Navier-Stokes equations for viscoelastic flow take the form

$$\frac{\partial u}{\partial t} + u_j \frac{\partial u_i}{\partial x_j} = -\frac{\partial p}{\partial x_i} + \frac{\beta}{\mathrm{Re}} \frac{\partial^2 u_i}{\partial x_j^2} + \frac{1-\beta}{\mathrm{Re}} \frac{\partial \tau_{ij}}{x_j}, \tag{1}$$

$$\frac{\partial u_i}{\partial x_i} = 0, \tag{2}$$

where Re is the Reynolds number, β is the ratio of the solvent to the total viscosity and $(1-\beta)$ is effectively a measure of the polymer concentration, and τ_{ij} is the polymer stress. This stress accounts for the interaction between the solvent and the polymer and depends on the conformation of the polymer chains, c_{ij}. The relationship between the polymer stress and the conformation for a FENE-P fluid is

$$\tau_{ij} = \frac{1}{\mathrm{Wi}} \left(\frac{c_{ij}}{\psi} - \frac{\delta_{ij}}{a} \right), \tag{3}$$

where the Weissenberg number Wi is the ratio of the polymer relaxation and the flow time scales, $\psi \equiv 1 - \frac{c_{kk}}{L^2}$ is the Peterlin function, $a \equiv 1 - \frac{3}{L^2}$, and L is the maximal extensibility of the polymers [20]. Finally, the conformation tensor satisfies the evolution equation,

$$\frac{\partial c_{ij}}{\partial t} + u_k \frac{\partial c_{ij}}{\partial x_k} = c_{kj} \frac{\partial u_i}{\partial x_k} + c_{ik} \frac{\partial u_j}{\partial x_k} - \tau_{ij}, \tag{4}$$

which includes advection by the velocity field, stretching due to the strain exerted on the polymer chains, and relaxation due to the elastic nature of the polymer.

Zhou and Akhavan [21] compared results for the preaveraged models with those for the FENE chain. They found the FENE-P closure to be in qualitative agreement. Furthermore, Stone *et al.* [22] found the FENE-P model to qualitatively capture the features of passive-bead spring chains in a complex turbulent flow field modeled using Brownian dynamics. For these reasons the model has been used extensively to simulate viscoelastic shear flows [23–25]. However, appropriate computational methods must be adopted to ensure stable and accurate simulations.

B. Numerical method

The hyperbolic nature of the conformation tensor evolution equation creates severe gradients in the conformation field, which can lead to numerical instabilities. Several numerical methods have been proposed to ensure stability and accuracy. For example, upwind schemes along with artificial diffusivity increase the stability of the numerical solution of hyperbolic equations [26]. In simulations of polymeric fluids with a maximum extensibility constraint, numerical errors can lead to predictions of polymer extensions that exceed their bounds. An implicit method to evaluate the conformation tensor equation, however, can resolve this problem [27].

The numerical method used in this work for the solution of the governing equations follows the approach by Min *et al.* [28,29]. We adopt a control-volume formulation for the spatial discretization, which has been widely tested for accurate simulations of transitional and turbulent flows [8,30]. The equations are advanced in time using a fractional-step algorithm where an implicit scheme (i.e., Crank-Nicolson) is adopted for the diffusion and the polymer stress terms, while the advection term is treated explicitly. A third-order upstream central scheme is used to compute the spatial derivatives of the conformation tensor in the longitudinal direction. A local artificial diffusivity is added at locations where the conformation tensor loses its positive definiteness to ensure numerical stability [28]. The additional term is $\kappa \Delta_k^2 \frac{\partial c_{ij}^2}{\partial^2 x_k}$, where Δ_k is the local grid spacing in the k direction [31]. The value of the coefficient κ should be sufficiently small. For the simulations presented here the choice $\kappa = 10^{-3}$ guarantees that the artificial diffusivity is inactive during the disturbance linear evolution and is restricted to less than 10% of the grid nodes during transition [31].

C. Simulation setup

We study dimensionless Couette flow (see Fig. 1). The height of the domain is $L_y = 2$ and the velocities at the walls are $U(\pm 1) = \pm U_w = \pm 1$. The base velocity profile is $\mathbf{U}(y,0,0)$ with corresponding conformation tensor $C_{xx} = \frac{1}{\psi(C_{kk})}(1 + \frac{2\mathrm{Wi}^2}{a^2\psi(C_{kk})^2})$, $C_{xy} = C_{yx} = \frac{\mathrm{Wi}}{a\psi^2(C_{kk})}$, and $C_{yy} = C_{zz} = \frac{1}{\psi(C_{kk})}$. Note that the other components are zero (see the Appendix for further details). The reference scales are the half-height of the domain $L_{\mathrm{ref}} = \frac{L_y}{2}$, the total viscosity of the fluid $\mu_{\mathrm{ref}} = \mu_S + \mu_P$, and the velocity at the upper wall, $U_{\mathrm{ref}} = U_w$. Based on these scales, the Reynolds number is $\mathrm{Re} \equiv \frac{U_w L_y}{2\nu} = 400$. Only one case with a different Re is analyzed. We vary both the Weissenberg number Wi and the polymer concentration β while the maximal extensibility of the polymers, L, is held constant: $L = 100$. Another important parameter is the extensibility, or the maximum value of the Trouton ratio [32]. In the present work, its influence is represented by changes in β since L is constant.

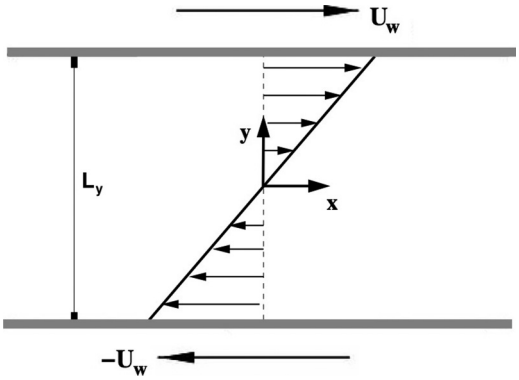

FIG. 1. Schematic of the computational setup.

Initial and boundary conditions

We report two classes of simulations: the first focuses on the evolution of the primary streaks (Sec. III) and the second examines the transition to turbulence (Sec. IV).

For the study of streak amplification, the initial condition is a Couette profile plus a streamwise vortex selected from the eigenspectrum of the Orr-Sommerfeld (OS) equations (see Ref. [17]) so that the initial condition reads

$$\mathbf{u}_i \equiv [y,0,0] + K[0, \underbrace{v_0(y,z), w_0(y,z)}_{O-S \quad \text{mode}}], \tag{5}$$

where $v_0(y,z)$ and $w_0(y,z)$ are the vertical and spanwise velocities,

$$v_0(y,z) = \cos(k_z z)\mathrm{Re}[\hat{v}(y)] - \sin(k_z z)\mathrm{Im}[\hat{v}(y)], \tag{6}$$

$$w_0(y,z) = \cos(k_z z)\mathrm{Re}[\hat{w}(y)] - \sin(k_z z)\mathrm{Im}[\hat{w}(y)], \tag{7}$$

and K controls the vortex amplitude. Note that the quantities $\hat{a}(y)$ represent the linear OS eigenmodes computed using the linear solver described by Zhang *et al.* [33]. The initial polymer conformation tensor is also defined by the sum of the base state and the OS eigensolution:

$$c_{xx,0}(y,z) = C_{xx} + K\cos(k_z z)\mathrm{Re}[\hat{c}_{xx}(y)] - K\sin(k_z z)\mathrm{Im}[\hat{c}_{xx}(y)], \tag{8}$$

$$c_{yy,0}(y,z) = C_{yy} + K\cos(k_z z)\mathrm{Re}[\hat{c}_{yy}(y)] - K\sin(k_z z)\mathrm{Im}[\hat{c}_{yy}(y)], \tag{9}$$

$$c_{xy,0}(y,z) = C_{xy} + K\cos(k_z z)\mathrm{Re}[\hat{c}_{xy}(y)] - K\sin(k_z z)\mathrm{Im}[\hat{c}_{xy}(y)], \tag{10}$$

$$c_{zz,0}(y,z) = C_{zz}, \quad \text{and} \quad c_{xz}(y,z) = c_{yz}(y,z) = 0. \tag{11}$$

For the second part of the study, the focus is placed on the secondary instability of the streak and breakdown to turbulence. Following the work by Cossu *et al.* [5], a sinuous secondary disturbance is introduced in the spanwise velocity when the primary streaks reach the highest amplitude. The secondary disturbance is

$$w_d(x,y) = (1-y^2)\sin(\alpha_d x), \tag{12}$$

where $\alpha_d = 0.7$. This value corresponds to the most unstable streamwise wavelength of the streak secondary instability in both Newtonian and viscoelastic Couette flow. The initial velocity of this second set of simulations is therefore

$$(u_i, v_i, w_i) = (u_s, v_s, w_s) + A_d[0,0,w_d(x,y)], \tag{13}$$

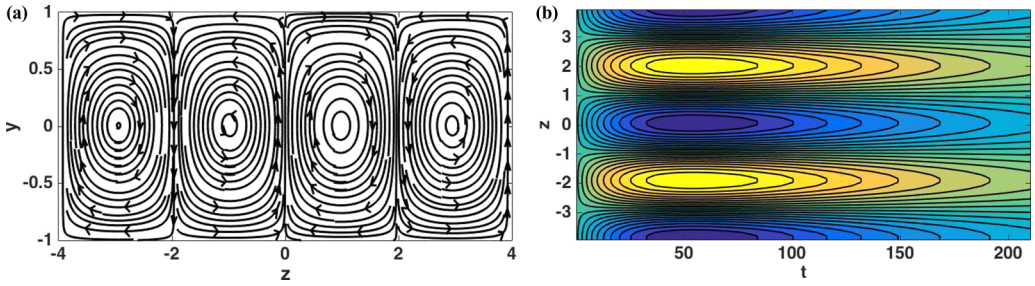

FIG. 2. (a) End view showing streamlines of the initial streamwise vortex. (b) Top view of the linear streak response, shown by contours of the streamwise velocity perturbation $-0.0071 \leqslant u' \leqslant 0.0071$.

where A_d is the amplitude of the secondary instability, and u_s, v_s, and w_s are the flow velocities from the first set of computations at the peak streak amplitude (see Sec. IV for more details).

Periodic boundary conditions are enforced in the streamwise and spanwise directions, while no-slip conditions are prescribed on the upper and lower walls.

D. Computational domain

Two different domain sizes were adopted for the nonlinear evolution of the primary streaks and the transition simulations, respectively. The grid was also adapted to the flow parameters since highly viscoelastic flows, i.e., high Wi or low β, can create sharp gradients in the polymer stress. As a result, these configurations required finer grids.

The numerical domain for simulating the primary streaks was $L_x = \pi$, $L_y = 2$, and $L_z = 2.5\pi$. The width L_z was chosen to accommodate the spanwise wave number of the initial streamwise vortices, $k_z = 1.6$. In this manner we have two periods of the mode along the z direction. The number of grid points in each direction depends on the flow under consideration. For Newtonian or low-viscoelastic cases we use $N_x = 8$, $N_y = 64$, and $N_z = 64$. However, as the Weissenberg number increases or β decreases we increase the number of grid points in the y and z directions up to four times, i.e., $N_y = 256$ and $N_z = 256$, while it is not necessary to increase the number of points along the x direction when dealing with streamwise independent disturbances.

As the sinuous secondary disturbance is introduced we set L_x to contain two streamwise wavelengths of the sinuous mode, i.e., $L_x = \frac{40}{7}\pi$. The domain size and the number of grid points were unchanged in the other two directions. Along the x direction we choose $N_x = 96$ for Newtonian and low-viscoelastic configurations. This value was increased up to fourfold in order to capture the dynamics at higher Wi.

III. EVOLUTION OF THE PRIMARY STREAKS

In this section we discuss the streak amplification in response to a streamwise vortex. As noted in Sec. II C, the vortex is an eigenmode of the viscoelastic Orr-Sommerfeld equation and is superimposed onto the Couette profile. The spanwise wave number of this mode is $k_z = 1.6$ and it corresponds to the optimal disturbance in a Newtonian Couette flow [3]. Streamlines of the initial vortex are shown in a cross-stream plane in Fig. 2(a). Due to the lift-up effect, the pair of counter-rotating streamwise vortices creates low- and high-speed streaks in the flow.

A. Linear evolution

For low amplitudes of the initial disturbance, its evolution will follow the linear behavior studied in Ref. [17]. Those authors defined three different regimes for the streamwise vortex mode in an Oldroyd-B fluid: quasi-Newtonian, elastic, and reenergization regimes. The range of parameters analyzed in the present work places it in the quasi-Newtonian regime.

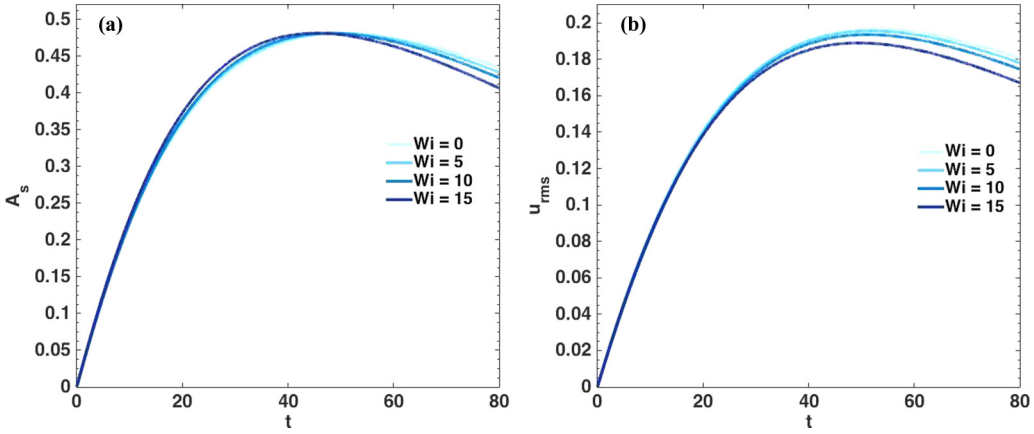

FIG. 3. Nonlinear evolution of the primary streak (a) A_s and (b) rms streamwise velocity $u_{\rm rms}$ for different Wi.

In Fig. 2(b) the linear evolution of the streak amplitude, i.e., the response to the streamwise vortex, is illustrated in the z-t plane for a Newtonian fluid. The streaks initially grow and eventually decay after reaching a maximum amplitude at time $t \approx 55$. The amplitude of the streak response is defined as $A_s = [\frac{1}{2}\frac{(u_{\rm max}-u_{\rm min})}{U_{\rm ref}}] \times 100$, where $u_{\rm max}$ and $u_{\rm min}$ are the instantaneous maximum and minimum of the streamwise velocity perturbation over the entire domain, $u(x,y,z) = u_{\rm tot}(x,y,z) - y$. The maximum in the streak amplitude also corresponds to a maximum in their total kinetic energy. A similar behavior is observed in viscoelastic flows. We have validated that our numerical simulations are in agreement with the linear response reported in Ref. [17].

B. Nonlinear evolution

Upon further increase of the initial amplitude of the streamwise vortex, K, the growth of the streaks is no longer linear. At nonlinear amplitudes, the streaks distort the base-flow profile, which in turn alters their growth rate. In addition, the generation of higher harmonics alters the shape of the disturbance field.

First, we define the *root mean square* (rms) of a generic observable $\phi_{\rm rms} = \sqrt{\overline{\phi^2}}$, where $\overline{\phi^2} = \int_{-\frac{L_z}{2}}^{\frac{L_z}{2}} \int_{-\frac{L_y}{2}}^{\frac{L_y}{2}} \int_{-\frac{L_x}{2}}^{\frac{L_x}{2}} \phi^2(x,y,z)\,dx\,dy\,dz$. The evolution of the amplitude A_s and the rms streamwise velocity $u_{\rm rms} = \sqrt{\overline{u^2}}$ is reported in Fig. 3 for different Weissenberg numbers and constant concentration, $\beta = 0.6$. In the figure, the Newtonian flow is indicated by the lightest color and increasing Weissenberg numbers are shown by darker lines; the darkest line corresponds to Wi = 15. As demonstrated by Fig. 3(a), the initial vortex amplitude K has been adjusted in order to have an equal maximum streak amplitude, $A_s = 48.13$, for all the viscoelastic conditions to be considered later. However, the maximum of $u_{\rm rms}$ is not equal among all configurations; it decreases with increasing elasticity. The difference can be attributed to the change in the streak shape with elasticity.

The mechanism causing the primary streak growth is vorticity tilting [3,4,34], which depends on the strain rate $\frac{\partial v}{\partial z}$ of the initial vortex. A measure of the strength of this process can be obtained from the streamwise vorticity. In addition, Page and Zaki [35] demonstrated that, in viscoelastic flows, a torque is exerted by the polymers onto the fluid $\boldsymbol{\chi} = \boldsymbol{\nabla} \wedge (\boldsymbol{\nabla} \cdot \boldsymbol{\tau})$ which has a resistive influence.

In Fig. 4 we illustrate the instantaneous streamwise vorticity (gray scale) and polymer torque (red and blue scales) at $t = 50$ for Wi $= 10$ and $\beta = 0.6$. The positive streamwise vorticity (white) is opposed by negative values of the torque (blue), while the negative vorticity (red) is opposed by a positive torque (blue), in agreement with previous results [35]. Figure 5 shows the time evolution of the *rms* streamwise vorticity $\omega_{x,\rm rms}$ and polymer torque $\chi_{x,\rm rms}$ for different values of Wi at $\beta = 0.6$. The streamwise vorticity decreases in time for all cases, at a faster rate when increasing the flow

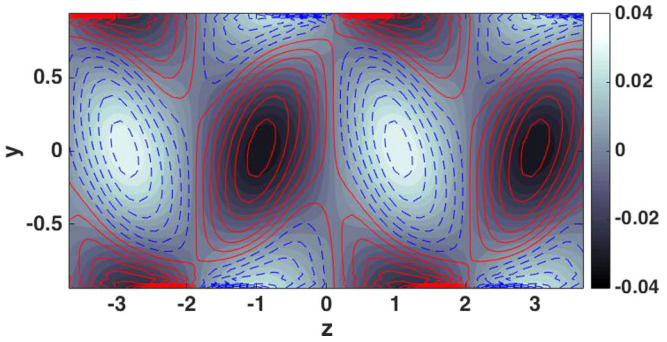

FIG. 4. Streamwise vorticity (gray scale) and polymer torque (red and blue lines) for Wi = 10, $\beta = 0.6$ at $t = 50$.

elasticity. While the streamwise torque also decays in time, its strength is appreciably increased with elasticity. This means that the polymers are weakening the streamwise vortices similarly to what was observed in the near-wall region in exact coherent structures of viscoelastic shear flows [36,37].

Figures 4 and 5 together can explain the reduction of the energy of the streak with increasing polymer relaxation time, Wi. Streak amplification is resisted by the streamwise polymer torque and this effect becomes more pronounced at higher Wi.

IV. TRANSITION TO TURBULENCE

In this section we analyze the effect of viscoelasticity on the secondary instability of streaks, which precedes breakdown to turbulence.

A. Secondary sinuous disturbance

As noted in Sec. II C, a secondary sinuous disturbance is introduced in the spanwise momentum equation as a Dirac delta function in time when the streak reaches its maximum amplitude [see Eq. (12)], similar to Ref. [5]. The wavelength α_d of this sinuous disturbance has to be carefully chosen. To this end, we have first conducted numerical simulations in longer domains (up to $L_x = 20\pi$) with a random disturbance of amplitude $A_d = 4$ to find the most unstable streamwise

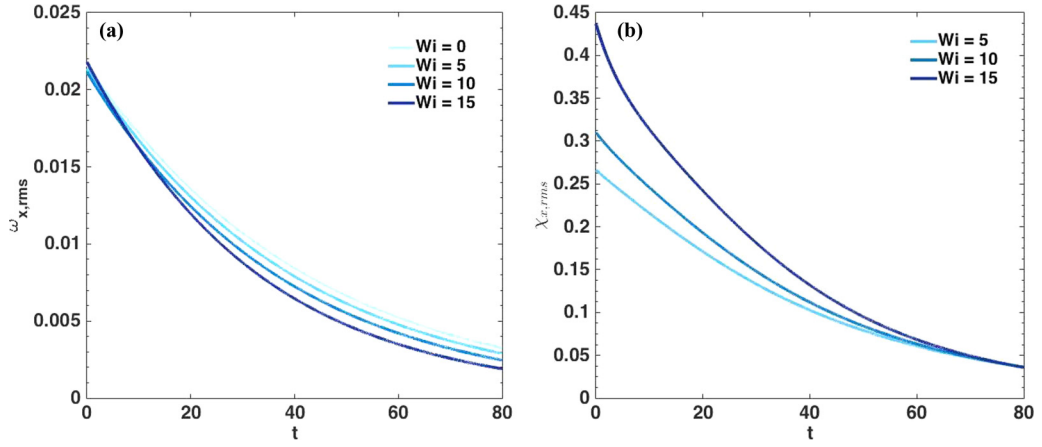

FIG. 5. Temporal evolution of the (a) rms streamwise vorticity $\omega_{x,\mathrm{rms}}$ and (b) rms streamwise polymer torque $\chi_{x,\mathrm{rms}}$ for different values of Wi for $\beta = 0.6$. Line colors retain the same designation as in Fig. 3.

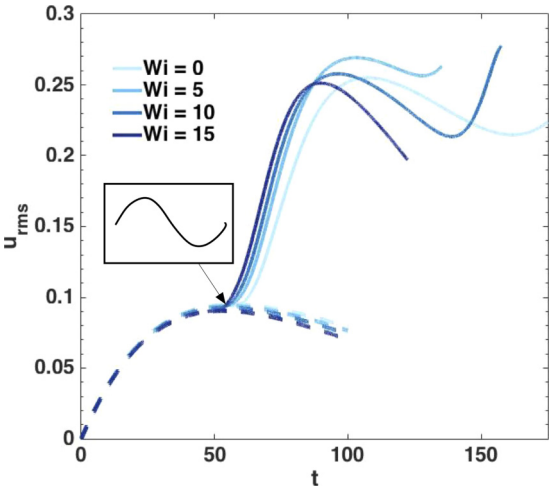

FIG. 6. The temporal evolution of the streamwise velocity disturbance, u_{rms}, for different Wi. Dashed curves show the evolution of the primary streaks created by the streamwise independent initial condition. Solid lines mark the disturbance evolution after the introduction of a sinuous forcing with amplitude $A_d = 12$. The amplitude of the streaks is $A_{s,\mathrm{in}} = 22.58$ when the sinuous forcing is introduced. Note that for Wi $= 15$ the streaks do not break down to turbulence.

wavelength. The wave number of the emerging instability was found to be approximately $\alpha_x = 0.7$. Additional tests were performed to check the dependence of this value on (i) the length of the domain L_x, (ii) the amplitude of the disturbance, A_d, and (iii) the viscoelasticity parameters (Wi and β), without significant variations. The wavelength of the sinuous forcing was therefore set to $\alpha_d = 0.7$.

The temporal evolution of the streamwise velocity disturbance, u_{rms}, for different Wi is depicted in Fig. 6 for the two types of simulations performed here. The evolution of the primary streaks created by the streamwise independent initial condition is indicated by dashed lines, and the disturbance evolution after the introduction of the sinuous forcing is marked by a continuous line. The sinuous forcing reinforces the disturbance, which continues to grow instead of decaying as was the case in Sec. III B. Transition to turbulence depends on the amplitude of the forcing, A_d: for lower amplitudes the streaks eventually decay after reaching a maximum energy.

B. Neutral curves

The transition scenario just discussed is bound to depend on $A_{s,\mathrm{in}}$, the amplitude of the primary streaks at the time when the sinuous forcing is introduced, and A_d, the amplitude of this sinuous disturbance. Here we evaluate the critical amplitude $A_{d,c}$ for which the streaks break down and initiate the turbulent regime. The results are illustrated in Figs. 7(a) and 7(c) for different values of Weissenberg number and concentration. In Fig. 7(a) the polymer concentration is set to $\beta = 0.6$ and the curves are plotted for different Wi. The data reveal that the streaks breakdown is favored for Wi $= 5$. This is more clearly seen in Fig. 7(b), where we rescale the neutral curves displayed in Fig. 7(a) with the Newtonian values. Indeed, the disturbance amplitude necessary to trigger the transition for Wi $= 5$ is reduced by 20% relative to the Newtonian case. This destabilization coincides with the regime where the exact coherent state is favored in viscoelastic Couette flow (Wi < 7) and where larger drag has been reported [36]. As Wi increases, however, the polymers have a stabilizing effect.

Interestingly at Wi $= 15$ we find a different behavior for low- and high-amplitude streaks. The presence of the polymer additives has always a stabilizing effect and transition occurs for higher disturbance amplitudes. However, the stabilization is significant for lower amplitude streaks,

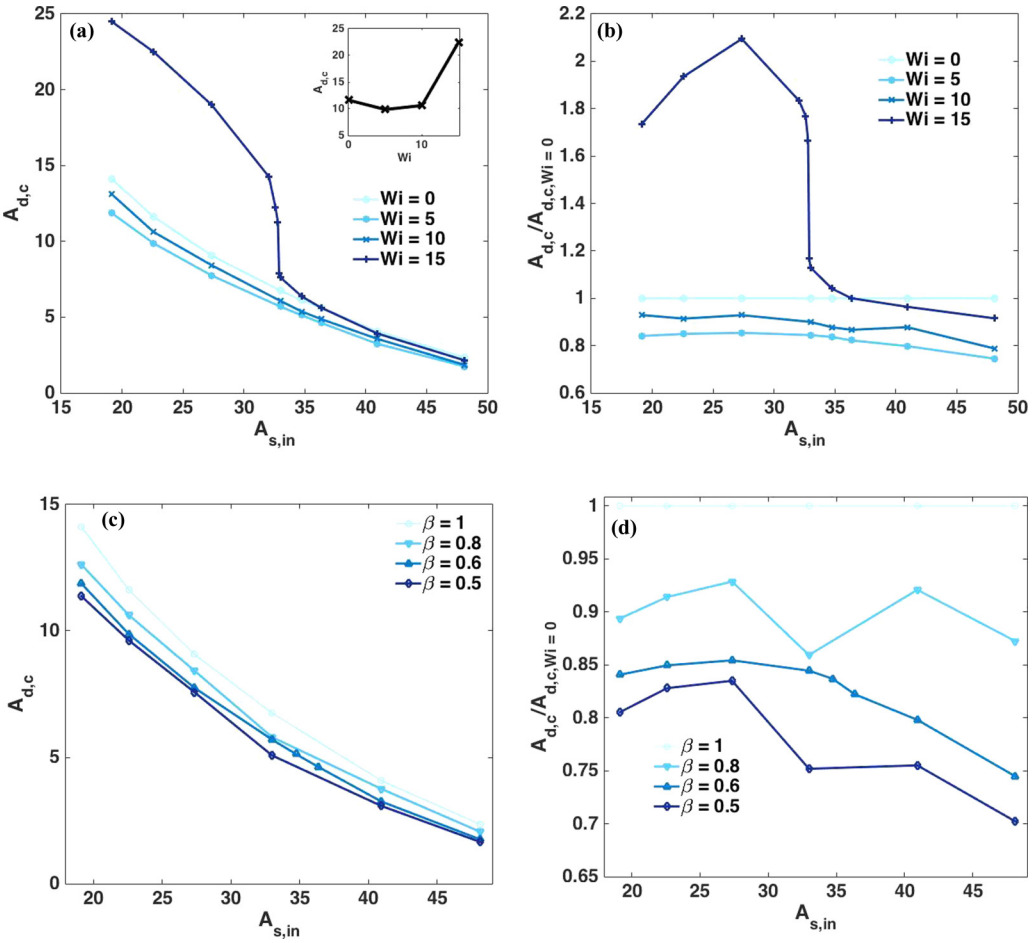

FIG. 7. (a) Neutral curves in the $(A_{s,\mathrm{in}}, A_d)$ plane for different values of Wi. The polymer concentration is $\beta = 0.6$. Inset of (a):$A_{d,c}$ vs Wi for $A_{s,\mathrm{in}} = 22.58$. (b) Neutral curves normalized by the Newtonian case. (c) Neutral curves in the $(A_{s,\mathrm{in}}, A_d)$ plane for different values of β. The Weissenberg number is Wi $= 5$. (d) Neutral curves normalized by the Newtonian case.

$A_{s,\mathrm{in}} < 0.35$, with up to 100% increase of the threshold amplitude, and vanishes at higher values of $A_{s,\mathrm{in}}$. We also highlight the nonmonotonic dependence of the transition thresholds on the Weissenberg number; see the inset in Fig. 7(a), where the critical disturbance amplitude $A_{d,c}$ is displayed versus Wi for $A_{s,\mathrm{in}} = 22.58$.

In Fig. 7(c) we trace the neutral curves with varying β while keeping the Weissenberg number constant (Wi $= 5$). The influence of viscoelasticity is always destabilizing. In Fig. 7(d) the neutral curves from Fig. 7(c) are normalized using the Newtonian values. For $\beta = 0.5$ the sinuous forcing strength is reduced up to 20–30% depending on the initial streak amplitude. In general we observe that the degree of destabilization is stronger for large $A_{s,\mathrm{in}}$.

C. Streak breakdown mechanisms

The significantly different behavior observed at small and large $A_{s,\mathrm{in}}$ is evident when comparing Figs. 6 and 8. These two figures report the temporal evolution of u_{rms} for two different streak amplitudes: $A_{s,\mathrm{in}} = 22.58$ and $A_{s,\mathrm{in}} = 48.13$. For the latter case, the disturbance starts growing

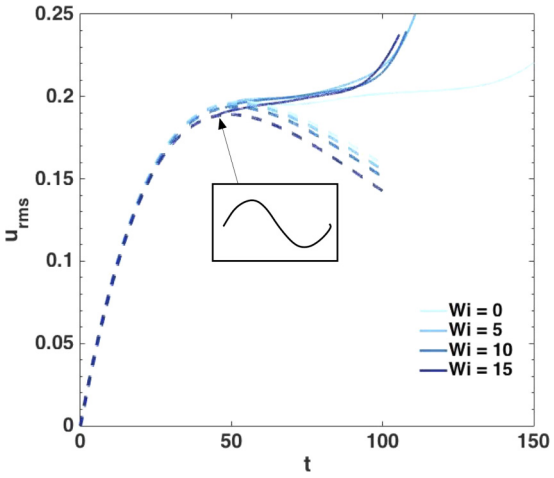

FIG. 8. The temporal evolution of the streamwise velocity disturbance, u_{rms}, for different Wi. Dashed curves show the evolution of the primary streaks created by the streamwise independent initial condition. Solid lines mark the disturbance evolution after the introduction of a sinuous forcing with amplitude $A_d = 2.4$. The amplitude of the streaks is $A_{s,\mathrm{in}} = 48.13$ when the sinuous forcing is introduced.

after the introduction of the sinuous forcing and the breakdown to turbulence follows directly if the disturbance is of sufficient amplitude. In contrast, for lower amplitude streaks, $A_{s,\mathrm{in}} = 22.58$ (Fig. 6), a distinct two-stage process is observed, similar to that described in previous studies [5,6,10]. In Fig. 9 we report the rms of the streamwise and wall-normal components of the vorticity [Fig. 9(a)] and the rms of the three components of velocity [Fig. 9(b)]. The perturbation due to the instantaneously imposed sinuous forcing [associated with the rms spanwise velocity; see Fig. 9(b)] initially decays, yet causes the growth of streamwise vortices (associated with streamwise vorticity and wall-normal velocity) that in turn induce the growth and breakdown of streaks. In other words, the streamwise periodic vorticity induced by the tilting of the initial wall-normal vorticity disturbance generates

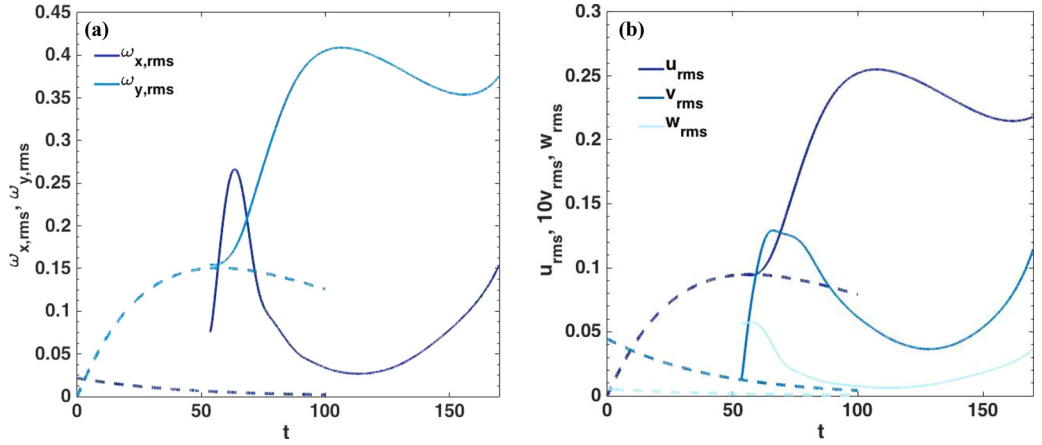

FIG. 9. The temporal evolution of (a) the streamwise and wall-normal rms vorticity and (b) the streamwise, wall-normal, and spanwise rms velocity for Wi = 0 and $A_{s,\mathrm{in}} = 22.58$. Dashed curves show the evolution of the primary streaks created by the streamwise independent initial condition. Solid lines mark the disturbance evolution after the introduction of a sinuous forcing with amplitude $A_d = 12$. The amplitude of the streaks is $A_{s,\mathrm{in}} = 22.58$ when the sinuous forcing is introduced.

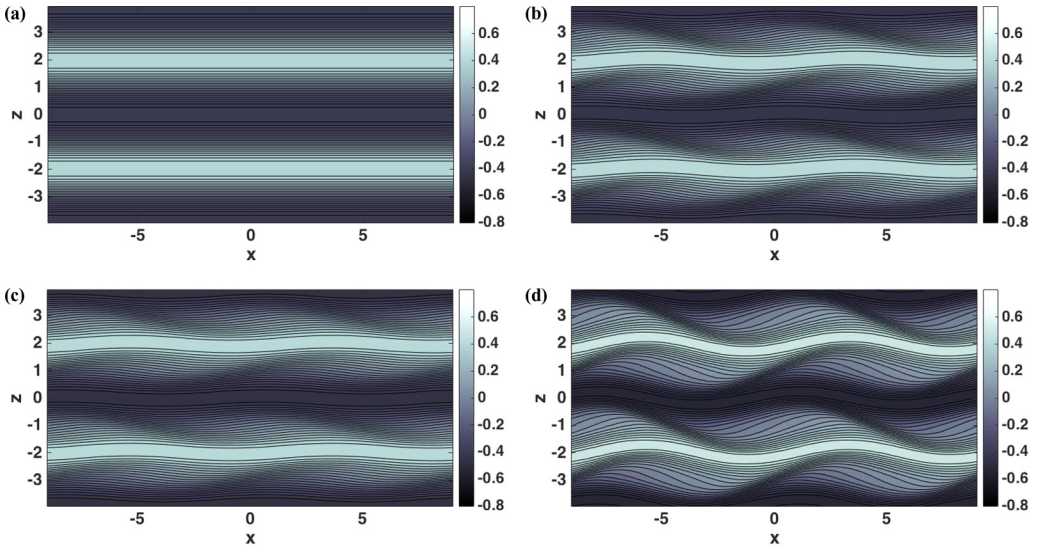

FIG. 10. Instantaneous contours of the streamwise velocity disturbance u in the x-z plane for the Newtonian case. The initial streak amplitude is $A_{s,\mathrm{in}} = 48.13$ while the sinuous disturbance amplitude is $A_d = 2.4$. The contours are evaluated at (a) $t' = 0$, (b) $t' = 20$, (c) $t' = 60$, and (d) $t' = 105$.

streaks of finite length, alternating in a periodic fashion in the streamwise direction. The streaks induced by these vortices also have a finite length and their breakdown to turbulence is associated with the interaction between a downstream low-speed region and an upstream high-speed region that generates strongly inflectional wall-normal profiles [8,30,38,39].

These two different mechanisms are visualized in Figs. 10 and 11, where we display contours of u in the wall-parallel x-z plane for the Newtonian case at different times $t' = t - t_d$, where

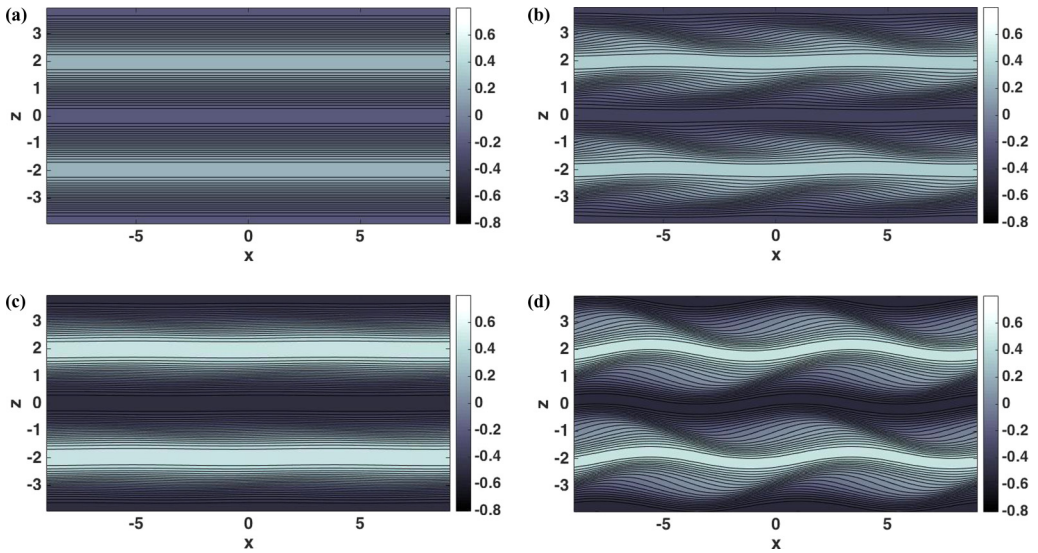

FIG. 11. Instantaneous contours of the streamwise velocity disturbance u in the x-z plane for the Newtonian case. The initial streak amplitude is equal to $A_{s,\mathrm{in}} = 22.58$ while the sinuous disturbance amplitude is $A_d = 12$. The contours are evaluated at (a) $t' = 0$, (b) $t' = 20$, (c) $t' = 60$, and (d) $t' = 120$.

t_d is the time at which the instantaneous sinuous forcing is applied. For $A_{s,\mathrm{in}} = 48.13$ the primary streaks monotonously deform under the effect of the forcing while growing in amplitude [Figs. 10(b) and 10(c)] and eventually break down to turbulence [Fig. 10(d)]. For small initial amplitudes, the streaks first bend [Fig. 11(b)] but eventually return to be almost straight [Fig. 11(c)]. Finally, the streaks are deformed again [Fig. 11(d)] and eventually break down to turbulence under the effect of the growth of the new streamwise vortices created by the forcing. It is important to highlight that the two mechanisms do not qualitatively vary when viscoelasticity is introduced.

D. Effect of the viscoelasticity

The previous section illustrated the two mechanisms that regulate the transition to turbulence for low- and high-amplitude streaks. Here we aim to explain the different degrees of stabilization that are observed at large Wi for low- (Sec. IV D 1) and high-amplitude (Sec. IV D 2) streaks.

1. Small initial primary streak amplitudes

To understand the effect of polymers, we consider the perturbation energy budget. The transport equation for the Reynolds stress in a viscoelastic flow is given by

$$\frac{\partial \overline{u_i' u_j'}}{\partial t} = \underbrace{-U_k \frac{\partial \overline{u_i' u_j'}}{\partial x_k}}_{\mathcal{A}_{ij}} \underbrace{-\frac{\partial \overline{u_i' u_j' u_k'}}{\partial x_k}}_{\mathcal{Q}_{ij}} \underbrace{-\left(\overline{u_j' \frac{\partial p'}{\partial x_i}} + \overline{u_i' \frac{\partial p'}{\partial x_j}}\right)}_{\mathcal{R}_{ij}}$$
$$\underbrace{-\left(\overline{u_j' u_k'} \frac{\partial U_i}{\partial x_k} + \overline{u_i' u_k'} \frac{\partial U_j}{\partial x_k}\right)}_{\mathcal{P}_{ij}} + \underbrace{\frac{\beta}{\mathrm{Re}} \frac{\partial^2 \overline{u_i' u_j'}}{\partial x_k^2}}_{\mathcal{D}_{ij}} \underbrace{-2\frac{\beta}{\mathrm{Re}} \overline{\frac{\partial u_i'}{\partial x_k} \frac{\partial u_j'}{\partial x_k}}}_{\epsilon_{ij}} + \underbrace{\frac{1-\beta}{\mathrm{Re}} \left(\overline{u_j' \frac{\partial \tau_{ik}'}{\partial x_k}} + \overline{u_i' \frac{\partial \tau_{jk}'}{\partial x_k}}\right)}_{\mathcal{W}_{ij}}, \tag{14}$$

where $\mathcal{A}_{ij}$ is advection by the mean flow, $\mathcal{Q}_{ij}$ is the transport by the velocity fluctuations, $\mathcal{R}_{ij}$ is the pressure redistribution, $\mathcal{P}_{ij}$ is the production against the mean shear, $\mathcal{D}_{ij}$ is viscous diffusion, ϵ_{ij} is dissipation, and $\mathcal{W}_{ij}$ is the polymer work. The evolution equation for the perturbation energy is obtained by setting $i = j$ in Eq. (14). First, by examining the terms in the energy budget we note that the influence of viscoelasticity is most pronounced in the energy production $\mathcal{P}_{ij}$, the viscous dissipation ϵ_{ij}, and the polymer work $\mathcal{W}_{ij}$. These are therefore the focus of the following analysis.

We first examine the $\overline{u'u'}$ energy budget since the streaks are associated with the streamwise velocity. In particular in Fig. 12 the energy production $\mathcal{P}_{xx}$ [Fig. 12(a)], viscous dissipation ϵ_{xx} [Fig. 12(b)], polymer work $\mathcal{W}_{xx}$ [Fig. 12(c)], and their sum [Fig. 12(d)] are plotted for different Wi. The maximum of the production is enhanced by the polymers, while the dissipation is damped. Most interestingly, the polymer work has a damping effect (i.e., the polymers extract energy from the flow) whose magnitude decreases when increasing Weissenberg number. The peak of the sum of the three components is, however, increasing with Wi, which indicates that the polymeric solution enhances the streak energy growth. Viscoelasticity thus has a destabilizing influence. While this trend is in agreement with the observations at low Wi, it cannot explain the behavior at large Wi. A similar approach explains the destabilization due to an increase in the polymer concentration observed [Figs. 7(c) and 7(d)] as a result of enhanced production.

The second, and important, growth of the streaks observed when the sinuous forcing is introduced at small $A_{s,\mathrm{in}}$ is due to the tilting of the wall-normal vorticity as explained in Sec. IV C. We therefore examine the effect of viscoelasticity on the evolution of the wall-normal vorticity in order to explain the stabilization shown for large Wi in Fig. 7. The contours of the wall-normal vorticity (gray scale) at $t' = 85$ for $\mathrm{Wi} = 10$, $\beta = 0.6$, $A_{s,\mathrm{in}} = 22.58$, and $A_d = 12$ in the x-z and z-y planes are illustrated

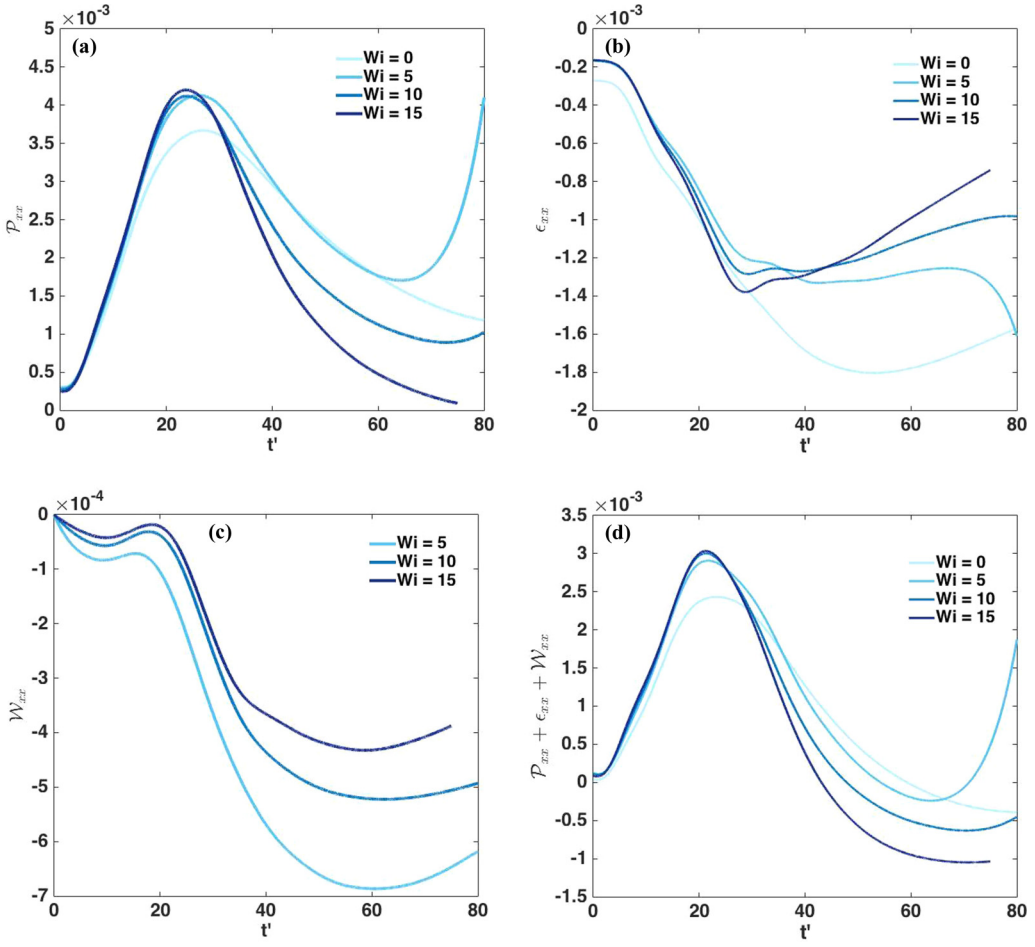

FIG. 12. Temporal evolution of the (a) energy production $\mathcal{P}_{xx}$, (b) dissipation ϵ_{xx}, (c) polymer work $\mathcal{W}_{xx}$, and (d) their sum for $A_{s,\mathrm{in}} = 22.58$ and $A_d = 12$.

in Figs. 13(a) and 13(b), respectively. Also plotted is the wall-normal polymer torque (see Sec. III B) in red and blue.

Cossu *et al.* [5] showed how the second maximum in u_{rms}, which was observed after introducing the sinuous forcing (see Fig. 6), is strictly related to a growth of the wall-normal vorticity. Figure 13

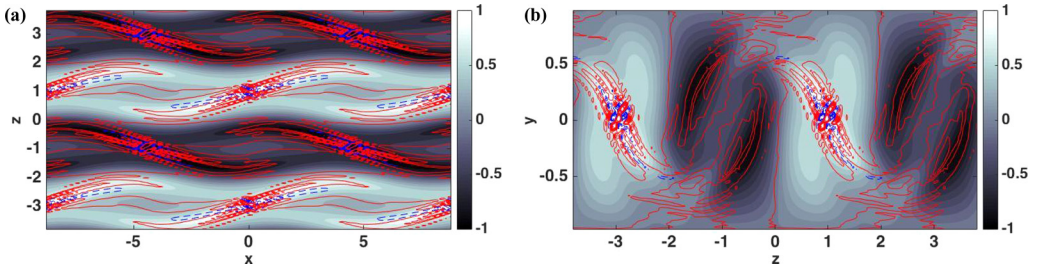

FIG. 13. Wall-normal vorticity (gray scale) and polymer torque (red and blue lines) for Wi $= 10$, $\beta = 0.6$, $A_{s,\mathrm{in}} = 22.58$, and $A_d = 12$ at $t' = 85$ in the (a) x-z and (b) z-y planes.

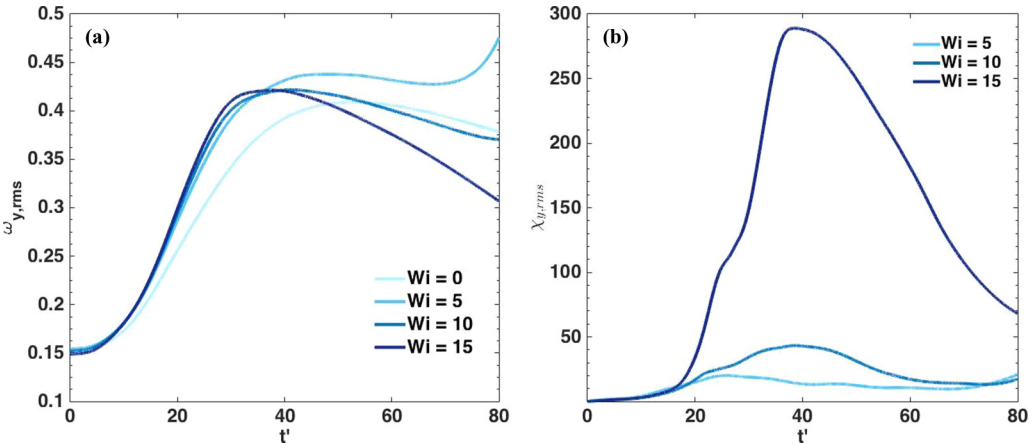

FIG. 14. Temporal evolution of the wall-normal component of the (a) rms vorticity and (b) rms polymer torque for $A_s = 22.58$, $A_d = 12$, and $\beta = 0.6$ at different Wi.

shows that the polymer torque has a resistive effect on the streaks by opposing the wall-normal vorticity, consistent with the results by Page and Zaki [35]. To quantify this effect, we report the rms of the wall-normal vorticity $\omega_{y,\mathrm{rms}}$ and wall-normal polymer torque $\chi_{y,\mathrm{rms}}$ in Fig. 14 at several Weissenberg numbers. The figure shows that the wall-normal vorticity initially increases with Weissenberg number, while it is damped as the viscoelastic effects start to be significant. On the other hand, the wall-normal polymer torque varies significantly with Wi. In particular, the peak value for Wi = 15 is more than ten times larger than that for Wi = 5. This substantial increase in the polymer torque is the main cause for the stabilization observed for weak initial streaks when increasing the Weissenberg number to Wi = 15.

2. *Large initial primary streak amplitudes*

For strong initial vortex amplitudes, the primary streaks are sufficiently energetic and unstable that they break down to turbulence directly when subjected to the weak sinuous forcing. This differs from the previous observations for low $A_{s,\mathrm{in}}$ where the transition to turbulence is due to a two-stage mechanism and the energy of the primary streaks is not crucial to explain the breakdown. We report in Fig. 15 the most relevant terms in the kinetic energy balance for a large-amplitude streak, $A_{s,\mathrm{in}} = 48.13$ and $A_d = 2.4$, similar to Fig. 12 for a streak of lower amplitude. The initial energy production [Fig. 15(a)] is damped by the polymers. This is consistent with the observation in Sec. III B that the peak in the average streak energy decreases when increasing Wi. The initial destabilization noticed in Fig. 7(a) at low Wi is due to the lower dissipation in viscoelastic flows relative to the corresponding Newtonian case, as shown in Fig. 15(b). The polymer work [cf. Fig. 15(c)] is negative but small during the initial stage. It is therefore not influential in the streak breakdown at high $A_{s,\mathrm{in}}$. As in Fig. 15(d), the sum of the three components $\mathcal{P}_{xx} + \epsilon_{xx} + \mathcal{W}_{xx}$ is a better indicator of whether transition to turbulence takes place.

The decrease in dissipation for the viscoelastic cases is related to the choice of the reference viscosity μ_{ref} used to calculate the Reynolds number [33]. We have chosen the total viscosity of the fluid as the reference value. If only the solvent viscosity is used, viscous dissipation would not decrease. This point is demonstrated in Fig. 16(a), where we have rescaled the viscous dissipation from Fig. 15(b) using the solvent viscosity, i.e., dividing the viscous dissipation by β. The initial viscous dissipation, once rescaled, is not significantly affected by the polymers. The Reynolds number based on the solvent viscosity for the viscoelastic cases in Fig. 15 is equal to $\mathrm{Re}_s = \frac{\mathrm{Re}}{\beta} = 666.67$. In Fig. 16(b) we compare the viscous dissipation of a Newtonian case with $\mathrm{Re} = \mathrm{Re}_s = 666.67$ to the viscoelastic configurations in Fig. 15(b). The solvent Reynolds number Re_s is constant

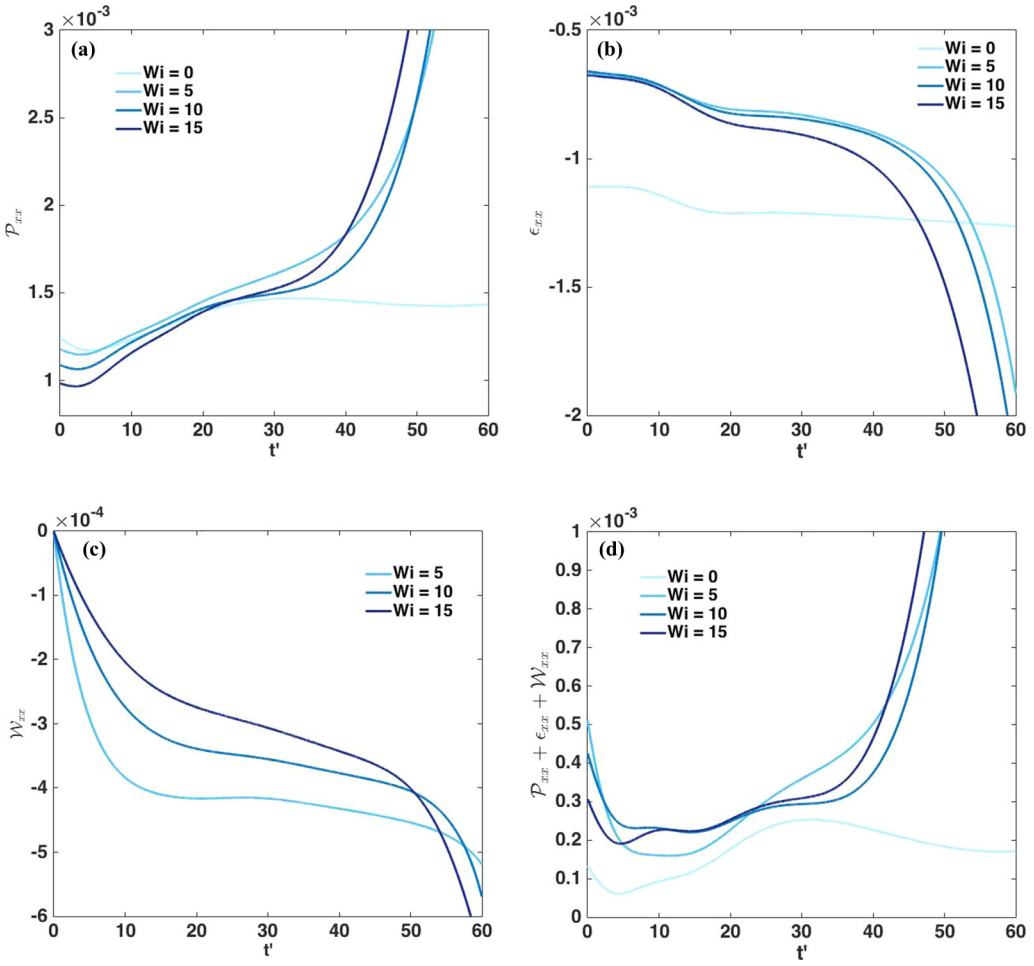

FIG. 15. Temporal evolution of the (a) energy production $\mathcal{P}_{xx}$, (b) dissipation ϵ_{xx}, (c) polymer work $\mathcal{W}_{xx}$, and (d) their sum for $A_{s,\text{in}} = 48.13$ and $A_d = 2.4$.

for all four cases ($\text{Re}_s = 666.67$). We note that the initial dissipation is inappreciably changed. These results point out how the destabilization at large initial streak amplitudes can be significantly affected by changes in the solvent viscosity. This differs from what is observed at small $A_{s,\text{in}}$, where the destabilization is created mainly by an increase in the energy production (see Sec. IV D 1).

We have previously seen how the polymer torque has a resistive effect on vorticity. In particular it plays a fundamental role in (i) lowering the energy of the primary streaks (Sec. III B) and (ii) hindering transition for small $A_{s,\text{in}}$ (Sec. IV D 1). For large $A_{s,\text{in}}$, the streak breakdown is accompanied by an increase of the streamwise vorticity [5]. The *rms* streamwise vorticity and polymer torque are illustrated in Fig. 17 for several values of the Weissenberg number, and large streak amplitude $A_s = 48.13$, sinuous forcing $A_d = 2.4$, and $\beta = 0.6$. The figure shows that the maximum of the streamwise vorticity increases with elasticity, while the polymer torque initially decreases with elasticity at short times. Note also that the polymer torque grows rapidly at large Wi. In summary, the polymer torque is lower than in the case of weak streaks [see Fig. 14(b)]. This explains why the streak breakdown is only slightly retarded in highly viscoelastic flows at large $A_{s,\text{in}}$, in contrast to small $A_{s,\text{in}}$.

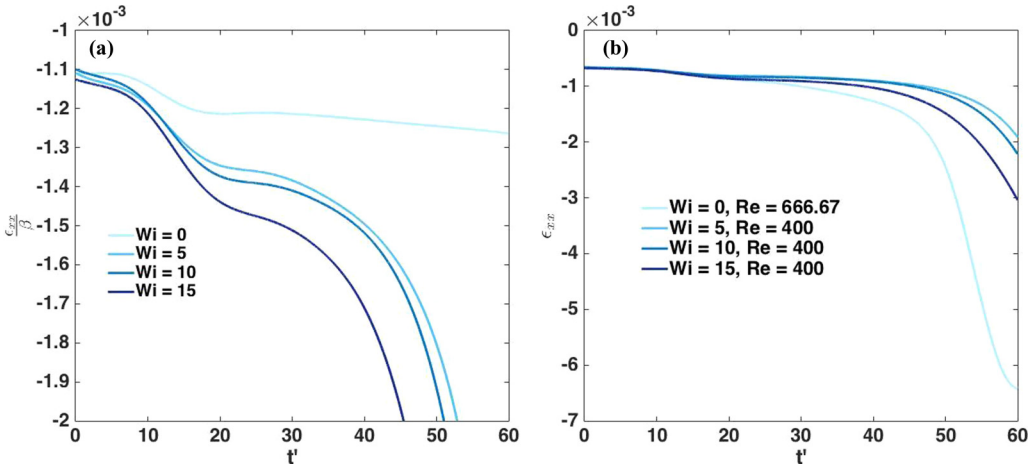

FIG. 16. (a) Viscous dissipation from Fig. 15(b) rescaled by the solvent viscosity instead of the total viscosity. (b) Comparison between the viscous dissipation of (i) the Newtonian case at $\mathrm{Re} = \mathrm{Re}_s = 666.67$ and (ii) the viscoelastic configurations from Fig. 15(b) where $\mathrm{Re} = 400$. The solvent Reynolds number is constant in all four cases: $\mathrm{Re}_s = 666.67$.

V. CONCLUSIONS

In this work we have examined the secondary instability of streaks and transition to turbulence in viscoelastic Couette flow. The polymeric solution was modeled using a FENE-P fluid, and the flow evolution evaluated using direct numerical simulations. The base streaks belong to the quasi-Newtonian regime according to the classification by Page and Zaki [17].

We have first studied the impact of elasticity on the nonlinear evolution of the streaks. The results show that the streaks reach a lower average energy with increasing elasticity. This is due to a resistive polymer torque that opposes the streamwise vorticity and, as a result, opposes the lift-up mechanism.

A streamwise-sinuous disturbance was introduced at the time when the streaks reached their maximum energy. The ensuant secondary instability was promoted (i) at low Wi and (ii) with increasing polymer concentration. However, at high Wi a change of trend is observed: transition to turbulence is delayed, and the degree of stabilization depends on the initial streak amplitude $A_{s,\mathrm{in}}$.

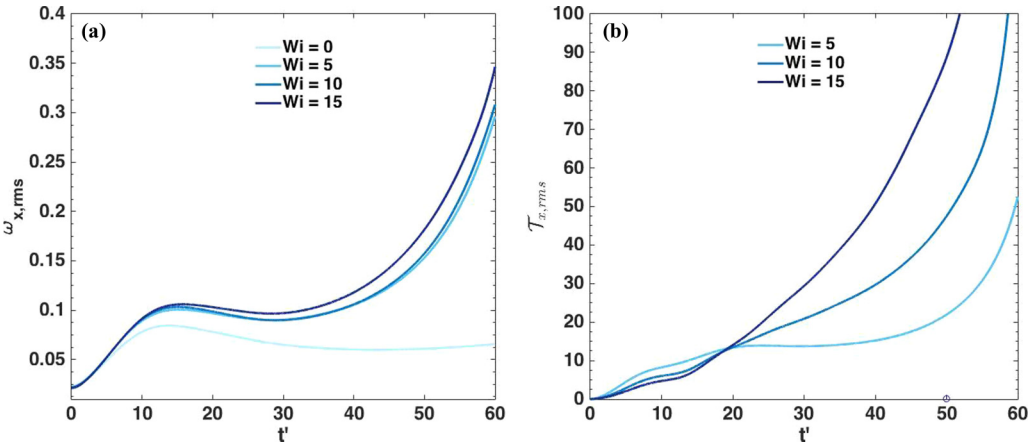

FIG. 17. Temporal evolution of the streamwise component of the (a) rms vorticity and (b) rms polymer torque for $A_s = 48.13$, $A_d = 2.4$, and $\beta = 0.6$ at different Wi.

If the streaks are weak we observe a sharp retardation of breakdown, and when they are strong, transition is only slightly delayed. The difference is due to a change in the transition mechanism at small and large $A_{s,\mathrm{in}}$. At small amplitudes transition takes place via a two-stage process, while at large amplitude the streaks directly break down when perturbed by the weak sinusoidal forcing. In both cases the stabilization at $\mathrm{Wi} = 15$ is due to a resistive polymer torque that opposes the growth of streaks. The cause of destabilization at low elasticity, on the other hand, depends on the streak amplitude:

(i) For small $A_{s,\mathrm{in}}$ and weak elasticity, transition is promoted due to an enhanced production. The pronounced perturbation growth leads to stronger, more unstable streaks that break down to turbulence.

(ii) For large $A_{s,\mathrm{in}}$ and weak elasticity, the solvent viscosity is effectively reduced, thus promoting streak instability and transition.

Similar arguments explain the destabilization caused by an increase in the polymer concentration.

Our findings can also have bearing on understanding drag reduction in wall-bounded polymeric turbulence [40]. The stabilizing influence of the polymer torque on streaks and its ability to delay breakdown to turbulence is consistent with earlier studies of the more complex, fully turbulent flows. There, the polymer torque was shown to limit the growth of vortical structures and inhibits the formation of hairpin packets and bursting events [41,42]. Xi and Graham [32] attributed the drag reduction in a minimal channel flow to the existence of time intervals of hibernating turbulence during which the streaks remain stable for relatively long times. The frequency and duration of these hibernating states increased at higher Weissenberg number. Analysis of the polymer torque and its role in initiating and sustaining these hibernating states can improve the current understanding of turbulent drag reduction.

It is interesting to consider a flow configuration where streaks appear with various sizes and amplitudes. For example, when a laminar boundary layer is exposed to broadband free-stream noise, Klebanoff streaks with different amplitudes and orientations amplify and their secondary instability [8,30,39] signals the onset of bypass transition to turbulence. The present analysis shows that the influence of elasticity, be it stabilizing or destabilizing, depends on the flow parameters. In addition, it is important to note that we focused on streaks that belong to the quasi-Newtonian class according to the classification by Page and Zaki [17]. Two other classes have been identified, namely, "elastic" and "reenergizing" streaks. In the former, streaks can reach very large amplitudes despite the weak inertia [18,19]. A similar DNS analysis in this regime could shed light on elastic turbulence [43,44]. The reenergization regime, on the other hand, occurs when the diffusion and relaxation time scales are commensurate and is characterized by a cyclical amplification of the base streaks within an envelope of growth and decay. Preliminary direct numerical simulations confirmed that this regime is observed in the full nonlinear problem. A complete study of these streaks and their secondary instability should be the subject of future work.

ACKNOWLEDGMENTS

This work is sponsored by the National Science Foundation under Grant No. 1511937. L. Biancofiore would also like to acknowledge support from the Marie Curie IEF-2012 Program under Grant PIEF-GA-2012-329424.

APPENDIX: ANALYTICAL EXPRESSION FOR THE BASE-STATE CONFORMATION TENSOR

In this section, we summarize the solution to Eq. (4) for the conformation tensor given a generic, parallel velocity profile $U(y)$. Using this base-flow ansatz, the conformation tensor can be

written as

$$c_{xx} = c_{yy}\left[1 + 2U'(y)^2\mathrm{Wi}^2\left(1 - \frac{3}{L^2}\right)c_{yy}^2\right], \tag{A1a}$$

$$c_{xy} = c_{yx} = U'(y)\mathrm{Wi}\left(1 - \frac{3}{L^2}\right)c_{yy}^2, \tag{A1b}$$

$$c_{yy} = c_{zz} = \frac{1 - \frac{c_{xx}+2c_{yy}}{L^2}}{1 - \frac{3}{L^2}}, \tag{A1c}$$

where $U'(y) = \frac{dU}{dy}$. If $L \to \infty$, the conformation tensor tends to the conformation tensor pertaining to an Oldroyd-B fluid: $c_{xx} = 1 + 2U'(y)^2\mathrm{Wi}^2$, $c_{xy} = c_{yx} = U'(y)\mathrm{Wi}$, and $c_{yy} = 1$. The base solution for the components of the conformation tensor can be obtained by inverting the above system, which yields

$$C_{xx} = \frac{1}{\psi(C_{kk})}\left[1 + \frac{2U'^2(y)\mathrm{Wi}^2}{a^2\psi(C_{kk})^2}\right], \tag{A2}$$

$$C_{xy} = \frac{U'(y)\mathrm{Wi}}{a\psi(C_{kk})^2}, \tag{A3}$$

$$C_{yy} = C_{zz} = \frac{1}{\psi(C_{kk})}, \tag{A4}$$

where $f(C_{kk}(j)) = \frac{2}{3}\cosh(\frac{\phi}{3}) + \frac{1}{3}$, $\phi = \mathrm{acosh}(\frac{27}{2}\Omega^2 + 1)$, and $\Omega = \sqrt{2}\frac{U'(y)\mathrm{Wi}}{aL}$. Dallas *et al.* [24] derived a similar expression but with a different choice of the Peterlin function. For the Couette flow studied in the present work $U'(y) = 1$ and, therefore,

$$C_{xx} = \frac{1}{\psi(C_{kk})}\left[1 + \frac{2\mathrm{Wi}^2}{a^2\psi(C_{kk})^2}\right], \tag{A5}$$

$$C_{xy} = \frac{\mathrm{Wi}}{a\psi^2(C_{kk})}, \tag{A6}$$

$$C_{yy} = C_{zz} = \frac{1}{\psi(C_{kk})}. \tag{A7}$$

[1] T. A. Zaki, From streaks to spots and on to turbulence: Exploring the dynamics of boundary layer transition, Flow Turbul. Combust. **91**, 451 (2013).

[2] M. T. Landahl, A note on an algebraic instability of inviscid parallel shear flows, J. Fluid Mech. **98**, 243 (1980).

[3] K. M. Butler and B. F. Farrell, Three-dimensional optimal perturbations in viscous shear flow, Phys. Fluids A **4**, 1637 (1992).

[4] L. Brandt, The lift-up effect: The linear mechanism behind transition and turbulence in shear flows, Eur. J. Mech. B Fluids **47**, 80 (2014).

[5] C. Cossu, L. Brandt, S. Bagheri, and D. S. Henningson, Secondary threshold amplitudes for sinuous streak breakdown, Phys. Fluids **23**, 074103 (2011).

[6] F. Waleffe, Hydrodynamic stability and turbulence: Beyond transients to a self-sustaining process, Stud. Appl. Math. **95**, 319 (1995).

[7] P. Andersson, L. Brandt, A. Bottaro, and D. S. Henningson, On the breakdown of boundary layer streaks, J. Fluid Mech. **428**, 29 (2001).
[8] N. J. Vaughan and T. A. Zaki, Stability of zero-pressure-gradient boundary layer distorted by unsteady Klebanoff streaks, J. Fluid Mech. **681**, 116 (2011).
[9] J. Hoepffner, L. Brandt, and D. S. Henningson, Transient growth on boundary layer streaks, J. Fluid Mech. **537**, 91 (2005).
[10] F. Waleffe, On a self-sustaining process in shear flows, Phys. Fluids **9**, 883 (1997).
[11] P. K. Ray and T. A. Zaki, Absolute instability in viscoelastic mixing layers, Phys. Fluids **26**, 014103 (2014).
[12] P. K. Ray and T. A. Zaki, Absolute/convective instability of planar viscoelastic jets, Phys. Fluids **27**, 014110 (2015).
[13] M. R. Jovanović and S. Kumar, Transient growth without inertia, Phys. Fluids **22**, 023101 (2010).
[14] B. K. Lieu, M. R. Jovanović, and S. Kumar, Worst-case amplification of disturbances in inertialess Couette flow of viscoelastic fluids, J. Fluid Mech. **723**, 232 (2013).
[15] E. S. G. Shaqfeh, Purely elastic instabilities in viscometric flows, Annu. Rev. Fluid Mech. **28**, 129 (1996).
[16] A. Agarwal, L. Brandt, and T. A. Zaki, Linear and nonlinear evolution of a localized disturbance in polymeric channel flow, J. Fluid Mech. **760**, 278 (2014).
[17] J. Page and T. A. Zaki, Streak evolution in viscoelastic Couette flow, J. Fluid Mech. **742**, 520 (2014).
[18] N. Hoda, M. R. Jovanović, and S. Kumar, Energy amplification in channel flows of viscoelastic fluids, J. Fluid Mech. **601**, 407 (2008).
[19] N. Hoda, M. R. Jovanović, and S. Kumar, Frequency responses of streamwise-constant perturbations in channel flows of Oldroyd-B fluids, J. Fluid Mech. **625**, 411 (2009).
[20] P. J. Oliveira, An exact solution for tube and slit flow of a FENE-P fluid, Acta Mech. **158**, 157 (2002).
[21] Q. Zhou and R. Akhavan, A comparison of FENE and FENE-P dumbbell and chain models in turbulent flow, J. Non-Newtonian Fluid Mech. **109**, 115 (2003).
[22] P. A. Stone and M. D. Graham, Polymer dynamics in a model of the turbulent buffer layer, Phys. Fluids **15**, 1247 (2003).
[23] Y. Dubief, C. M. White, V. E. Terrapon, E. S. G. Shaqfeh, P. Moin, and S. K. Lele, On the coherent drag-reducing and turbulence-enhancing behaviour of polymers in wall flows, J. Fluid Mech. **514**, 271 (2004).
[24] V. Dallas, J. C. Vassilicos, and G. F. Hewitt, Strong polymer-turbulence interactions in viscoelastic turbulent channel flow, Phys. Rev. E **82**, 066303 (2010).
[25] D. Richter, G. Iaccarino, and E. S. G. Shaqfeh, Simulations of three-dimensional viscoelastic flows past a circular cylinder at moderate Reynolds numbers, J. Fluid Mech. **651**, 415 (2010).
[26] R. Sureshkumar and A. N. Beris, Effect of artificial stress diffusivity on the stability of numerical calculations and the flow dynamics of time-dependent viscoelastic flows, J. Non-Newtonian Fluid Mech. **60**, 53 (1995).
[27] T. Vaithianathan and L. R. Collins, Numerical approach to simulating turbulent flow of a viscoelastic polymer solution, J. Comput. Phys. **187**, 1 (2003).
[28] T. Min, J. Y. Yoo, and H. Choi, Effect of spatial discretization schemes on numerical solutions of viscoelastic fluid flows, J. Non-Newtonian Fluid Mech. **100**, 27 (2001).
[29] T. Min, H. Choi, and J. Y. H. Yoo, Maximum drag reduction in a turbulent channel flow by polymer additives, J. Fluid Mech. **492**, 91 (2003).
[30] M. J. P. Hack and T. A. Zaki, Streak instabilities in boundary layers beneath free-stream turbulence, J. Fluid Mech. **741**, 280 (2014).
[31] Y. Dubief, V. E. Terrapon, C. M. White, E. S. G. Shaqfeh, P. Moin, and S. K. Lele, New answers on the interaction between polymers and vortices in turbulent flows, Flow Turbul. Combust. **74**, 311 (2005).
[32] L. Xi and M. D. Graham, Active and Hibernating Turbulence in Minimal Channel Flow of Newtonian and Polymeric Fluids, Phys. Rev. Lett. **104**, 218301 (2010).
[33] M. Zhang, I. Lashgari, T. A. Zaki, and L. Brandt, Linear stability analysis of channel flow of viscoelastic Oldroyd-B and FENE-P fluids, J. Fluid Mech. **737**, 249 (2013).

[34] T. A. Zaki and P. A. Durbin, Mode interaction and the bypass route to transition, J. Fluid Mech. **531**, 85 (2005).
[35] J. Page and T. A. Zaki, The dynamics of spanwise vorticity perturbations in homogeneous viscoelastic shear flow, J. Fluid Mech. **777**, 327 (2015).
[36] P. A. Stone, A. Roy, R. G. Larson, F. Waleffe, and M. D. Graham, Polymer drag reduction in exact coherent structures of plane shear flow, Phys. Fluids **16**, 3470 (2004).
[37] W. Li and M. D. Graham, Polymer induced drag reduction in exact coherent structures of plane Poiseuille flow, Phys. Fluids **19**, 083101 (2007).
[38] L. Brandt and H. C. De Lange, Streak interactions and breakdown in boundary layer flows, Phys. Fluids **20**, 024107 (2008).
[39] M. J. P. Hack and T. A. Zaki, Data-enabled prediction of streak breakdown in pressure-gradient boundary layers, J. Fluid Mech. **801**, 43 (2016).
[40] M. D. Graham, Drag reduction in turbulent flow of polymer solutions, Rheol. Rev. **2**, 143 (2004).
[41] K. Kim, C.-F. Li, R. Sureshkumar, S. Balachandar, and R. J. Adrian, Effects of polymer stresses on eddy structures in drag-reduced turbulent channel flow, J. Fluid Mech. **584**, 281 (2007).
[42] K. Kim and R. Sureshkumar, Spatiotemporal evolution of hairpin eddies, Reynolds stress, and polymer torque in polymer drag-reduced turbulent channel flows, Phys. Rev. E **87**, 063002 (2013).
[43] A. Groisman and V. Steinberg, Elastic turbulence in a polymer solution flow, Nature (London) **405**, 53 (2000).
[44] R. G. Larson, Fluid dynamics: Turbulence without inertia, Nature (London) **405**, 27 (2000).